Modeling and Robust Continuous TSM Control for an Inertially Stabilized Platform With Couplings

Jianliang Mao, Jun Yang, *Senior Member, IEEE*, Xiangyang Liu, Shihua Li, *Senior Member, IEEE*, and Qi Li

***Abstract*— Inertially stabilized platforms (ISPs), typically involving two or three axis gimbal, are extensively utilized to achieve accurate tracking of optical axis regardless of vehicle motion or vibration. Due to the complex nonlinearities induced by cross-couplings, parameter uncertainties, and external disturbances, high-performance control for ISPs is always a challenging task for practical applications, especially when the dynamic mass imbalance exists. In this brief, the situation that the mass distribution of an ISP is nonsymmetrical with respect to the mass center is emphatically analyzed, where the couplings are modeled and resolved into the known and unknown parts. To cope with the unmeasured states as well as the uncertainties composed of unknown couplings and remaining dynamics that are unmodeled, a higher order sliding mode observer (HOSMO) is developed for both the states and the lumped uncertainties estimation. By incorporating the estimated information, a robust continuous terminal sliding mode (TSM) control law is synthesized to admit the desired inertial angular rates tracking in finite time without offset. The validity of the presented control approach is demonstrated by experimental studies.**

***Index Terms*— Continuous terminal sliding mode control (CTSMC), cross-couplings, disturbance rejection control, higher order sliding mode observer (HOSMO), inertially stabilized platform (ISP).**

I. Introduction

OPTICAL-ELECTRONIC TRACKING SYSTEM (OETS) has been playing a crucial role in commercial, scientific, and military applications, such as environmental monitoring, missile guidance, target tracking, astronomical telescopes, etc., [1], [2]. In order to keep the light of sight (LOS) of the optical sensors insensitive to the effects of vehicle motion or vibration, inertially stabilized platforms (ISPs) are widely utilized in these applications. As shown in Fig. 1, a typical control framework of the OETS is usually composed of two feedback control loops, i.e., tracking and stabilized ones [3]. The outer loop aims to track the target by using visual signals and generates the desired angular rate for the inner loop, whereas the inner loop utilizes gyro signals to realize the inertial stabilization on both pitch and yaw channels. To improve the dynamic response and the disturbance rejection performance, we focus on the stabilization controller synthesis for the inner loop in this brief.

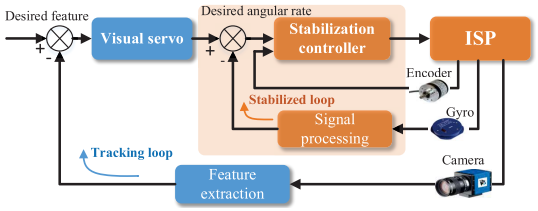

Fig. 1. Control framework of the OETS.

As a multi-degree-of-freedom electromechanical device, the ISP is essentially a highly nonlinear and intensively coupled system [4]. Rigorous modeling of an ISP is of great guidance to the high-performance control. With a sketchy overview of the development of the control strategies for the ISP system, the existing control methods can be classified into the following two categories. The first category mainly focuses on the advanced control algorithm design for the torque motor but ignores the complex nonlinearities such as cross-couplings and mass imbalance during the modeling process [5], [6]. Such a simplified treatment has largely facilitated the controller design but will cause the control performance degradation when there exist frequently rapid variations in system dynamics. By taking into account the relative rotations among pitch, yaw, and base gimbals, another category of ISP modeling is expressed by means of Newton–Euler theory or Lagrange equation [7]–[9]. The dynamic models are generally derived based upon the assumption that the gimbal mass distribution is symmetrical with respect to the mass center, i.e., the product of inertia (POI) is taken as zero. Nevertheless, even in a well-designed gimbal system, the dynamic mass imbalance exists due to the asymmetry of mass distribution [10], especially when the external payload is imposed. As such, the control performance is expected to be improved if these uncertain dynamics are explicitly considered for the stabilization controller development.

To improve the control performance in the presence of various disturbances and uncertainties, numerous kinds of control approaches such as neural network control [7], [8], internal mode control [9], sliding mode control (SMC) [11], and

Manuscript received April 21, 2019; revised July 3, 2019; accepted July 28, 2019. Date of publication August 23, 2019; date of current version October 9, 2020. Manuscript received in final form July 31, 2019. This work was supported in part by the National Nature Science Foundation of China under Grant 6197021872, Grant 61573099, Grant 61750110525, and Grant 61633003. Recommended by Associate Editor E. Usai. *(Corresponding author: Jun Yang.)*

J. Mao is with the School of Automation, Southeast University, Nanjing 210096, China, also with the Key Laboratory of Measurement and Control of CSE, Ministry of Education, Nanjing 210096, China, and also with the Research and Development Institute, Estun Automation Co., Ltd., Nanjing 211106, China (e-mail: mjl@seu.edu.cn).

J. Yang, X. Liu, S. Li, and Q. Li are with the School of Automation, Southeast University, Nanjing 210096, China, and also with the Key Laboratory of Measurement and Control of CSE, Ministry of Education, Nanjing 210096, China (e-mail: j.yang84@seu.edu.cn; xy_liu@seu.edu.cn; lsh@seu.edu.cn; liqikj@hotmail.com).

Color versions of one or more of the figures in this article are available online at http://ieeexplore.ieee.org.

Digital Object Identifier 10.1109/TCST.2019.2933382

active disturbance rejection control (ADRC) [10], [12], [13] have been investigated for the ISP system. However, the controllers presented above can only guarantee the inertial angular rate track the reference value asymptotically rather than in finite time. In reality, the finite-time stable system exhibits two remarkable superiorities: faster convergence rate around the equilibrium point and better disturbance rejection performance, which has attracted considerable attention in recent years [14]–[16]. As a kind of finite-time control scheme, the continuous terminal SMC (CTSMC) is put forward by [17] to resolve the high-frequency chattering issue in the traditional terminal SMC (TSMC) method [18]. It has been verified that the CTSMC approach not only possesses finite-time convergence property but also generates a continuous control signal which is conducive to the actuator implementation [19]–[23]. Nevertheless, these methods are only applicable to the case when all the plant states are physically measurable. In the general ISP system driven by torque motors, while the angular rates of the pitch and yaw gimbals can be measured by fiber optical gyroscope (FOG), obtaining the remaining unmeasured states (i.e., angular accelerations and motor currents) without additional sensors is not a trivial task [10].

In this brief, inspired by the design philosophy of disturbance observer-based control approach [24]–[27], a robust CTSMC is proposed for the high-precision applications of an ISP system. A comprehensive dynamic model taking into account mass imbalance and crossing-couplings is first derived, where the couplings are resolved into the known and unknown parts. To cope with the unmeasured states as well as the uncertainties arising from unknown couplings and other unmodeled dynamics including parameter variations and external disturbances, a higher order sliding mode observer (HOSMO) is constructed for both the states and the lumped uncertainties estimation. By incorporating the estimated information, a new terminal sliding surface is designed and an output-feedback-based CTSMC law is further synthesized to realize the offset-free tracking of inertial angular rates in finite time. Comparative experiments are conducted to verify the effectiveness of the proposed control scheme. To conclude, the main contributions of this brief are twofold.

1) *Complex nonlinearities such as cross-couplings and mass imbalance are explicitly taken into account for the controller design, which reduces the online observation burden of the designed sliding mode observer and, thus, improves the tracking accuracy of the system output.*
2) *In comparison with the conventional TSMC method, by utilizing the joint estimations of system states and uncertain dynamics, a new output-feedback nonlinear SMC approach is developed to address the disturbance rejection problem for the ISPs when the angular accelerations and motor currents are unavailable.*

II. Model Description and Problem Formulation

A. Configuration and Notations

The detailed hardware configuration of the two-axis ISP system is shown in Fig. 2. To realize the stabilization of the camera, a two-axis FOG fixed on the inner gimbal is utilized to measure the inertial angular rates on both yaw and pitch

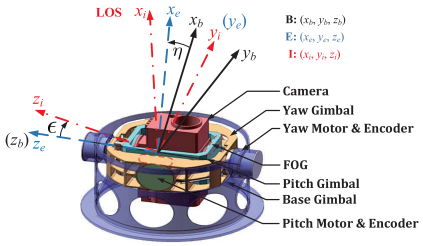

Fig. 2. Hardware configuration.

channels of pitch gimbal. Two permanent-magnet dc (PMDC) motors are applied as the direct-drive devices on account of their high torque when operating at a low speed. In addition, two encoders are mounted on the pitch and yaw gimbals, respectively, to provide the relative angles.

In Fig. 2, three reference frames are introduced: the base frame {B}, the outer frame {E}, and the inner frame {I}, where (x_b, y_b, z_b), (x_e, y_e, z_e), and (x_i, y_i, z_i) are the coordinate axes of {B}, {E}, and {I}, respectively. All the centers of rotation for three frames are assumed to be located in the coordinate origin. Furthermore, y_i is supposed to coincide with y_e-axis and z_b is supposed to coincide with z_e-axis. For neatness of expressions, some notations are introduced.

1) p_b, q_b, r_b Roll, pitch, and yaw components of the inertial angular rate vector ω_B in {B}, respectively.
2) p_e, q_e, r_e Roll, pitch, and yaw components of the inertial angular rate vector ω_E in {E}, respectively.
3) p_i, q_i, r_i Roll, pitch, and yaw components of the inertial angular rate vector ω_I in {I}, respectively.
4) η Rotational angle from {B} to {E} about the z_b-axis.
5) ϵ Rotational angle from {E} to {I} about the y_e-axis.
6) $\boldsymbol{R}_B^E$ Transformation matrix from {B} to {E}.
7) $\boldsymbol{R}_E^I$ Transformation matrix from {E} to {I}.

Under the definitions, the angular rate kinematics of the pitch and yaw gimbals can be expressed as

$$\begin{bmatrix} p_i \\ q_i \\ r_i \end{bmatrix} = \boldsymbol{R}_E^I \cdot \begin{bmatrix} p_e \\ q_e \\ r_e \end{bmatrix} + \begin{bmatrix} 0 \\ \dot{\epsilon} \\ 0 \end{bmatrix}, \quad \begin{bmatrix} p_e \\ q_e \\ r_e \end{bmatrix} = \boldsymbol{R}_B^E \cdot \begin{bmatrix} p_b \\ q_b \\ r_b \end{bmatrix} + \begin{bmatrix} 0 \\ 0 \\ \dot{\eta} \end{bmatrix} \tag{1}$$

where

$$\boldsymbol{R}_E^I = \begin{bmatrix} \cos\epsilon & 0 & -\sin\epsilon \\ 0 & 1 & 0 \\ \sin\epsilon & 0 & \cos\epsilon \end{bmatrix}, \quad \boldsymbol{R}_B^E = \begin{bmatrix} \cos\eta & \sin\eta & 0 \\ -\sin\eta & \cos\eta & 0 \\ 0 & 0 & 1 \end{bmatrix}.$$

Here q_i and r_i are available by using the mounted FOG, which are also the system variables we need to control.

B. ISP Dynamics

Assuming that each gimbal of the two-axis ISP system is a rigid body and the inertial matrices of the pitch and yaw gimbals are denoted by $\boldsymbol{J}_I \in \mathbb{R}^{3\times3}$ and $\boldsymbol{J}_E \in \mathbb{R}^{3\times3}$, respectively, given as

$$\boldsymbol{J}_I = \begin{bmatrix} J_{ix} & D_{xy} & D_{xz} \\ D_{xy} & J_{iy} & D_{yz} \\ D_{xz} & D_{yz} & J_{iz} \end{bmatrix}, \quad \boldsymbol{J}_E = \begin{bmatrix} J_{ex} & d_{xy} & d_{xz} \\ d_{xy} & J_{ey} & d_{yz} \\ d_{xz} & d_{yz} & J_{ez} \end{bmatrix}. \tag{2}$$

Remark 1: $D_{xy}, D_{xz}, D_{yz}, d_{xy}, d_{xz}, d_{yz}$ are called the gimbal POI originated from the dynamic mass imbalance. If the

mass distributions of both the gimbals are symmetrical with respect to the mass center (coordinate origin), POI are usually taken as zero.

1) Pitch Gimbal Dynamics: According to the Newton–Euler equation, for the pitch gimbal, we have

$$\boldsymbol{T}_I = d\boldsymbol{H}_I/dt + \omega_I \times \boldsymbol{H}_I \tag{3}$$

where $\boldsymbol{T}_I = [T_{ix}, T_{iy}, T_{iz}]^{\mathrm{T}} \in \mathbb{R}^3$ is the total external torque imposed on the pitch gimbal, $\omega_I = [p_i, q_i, r_i]^{\mathrm{T}} \in \mathbb{R}^3$ is the pitch gimbal angular rate, and $\boldsymbol{H}_I$ is the pitch gimbal angular momentum, denoted as $\boldsymbol{H}_I = \boldsymbol{J}_I\omega_I$.

By substituting (1) and (2) into (3), one obtains

$$T_{iy} = J_{iy}\dot{q}_i + T_{n1} + T_{d1} \tag{4}$$

where T_{n1} and T_{d1} denote the known and unknown cross-coupling dynamics caused by the rotations of base and yaw gimbals, respectively, which are given as

$$\begin{aligned} T_{n1} &= D_{yz}\dot{r}_i + D_{xy}q_ir_i + D_{xz}r_i^2 \\ T_{d1} &= (J_{ix} - J_{iz})p_ir_i - D_{xz}p_i^2 + D_{xy}\dot{p}_i - D_{yz}p_iq_i. \end{aligned} \tag{5}$$

2) Yaw Gimbal Dynamics: Similarly, the moment equation of the yaw gimbal can be presented as

$$\boldsymbol{T}_E = d\boldsymbol{H}_E/dt + \omega_E \times \boldsymbol{H}_E \tag{6}$$

where $\boldsymbol{T}_E = [T_{ex}, T_{ey}, T_{ez}]^{\mathrm{T}} \in \mathbb{R}^3$ is the total external torque imposed on the yaw gimbal, $\omega_E = [p_e, q_e, r_e]^{\mathrm{T}} \in \mathbb{R}^3$ is the yaw gimbal angular rate, and $\boldsymbol{H}_E$ is the yaw gimbal angular momentum, denoted as

$$\boldsymbol{H}_E = \bar{\boldsymbol{J}}_E\omega_E + \left(\boldsymbol{R}_E^I\right)^{\mathrm{T}}\boldsymbol{J}_I[0, \dot{\epsilon}, 0]^{\mathrm{T}}. \tag{7}$$

where $\bar{\boldsymbol{J}}_E$ is the inertial matrix of the total gimbal system with respect to the frame E, given by $\bar{\boldsymbol{J}}_E = \boldsymbol{J}_E + (\boldsymbol{R}_E^I)^{\mathrm{T}}\boldsymbol{J}_I\boldsymbol{R}_E^I$. Let $\bar{\boldsymbol{J}}_E := [\bar{J}_{ex}, \bar{d}_{xy}, \bar{d}_{xz}; \bar{d}_{xy}, \bar{J}_{ey}, \bar{d}_{yz}; \bar{d}_{xz}, \bar{d}_{yz}, \bar{J}_{ez}]$, then

$$\begin{aligned} \bar{J}_{ex} &= J_{ex} + J_{ix}\cos^2\epsilon + J_{iz}\sin^2\epsilon + D_{xz}\sin(2\epsilon) \\ \bar{J}_{ey} &= J_{ey} + J_{iy} \\ \bar{J}_{ez} &= J_{ez} + J_{ix}\sin^2\epsilon + J_{iz}\cos^2\epsilon - D_{xz}\sin(2\epsilon) \\ \bar{d}_{xy} &= d_{xy} + D_{xy}\cos\epsilon + D_{yz}\sin\epsilon \\ \bar{d}_{xz} &= d_{xz} + (J_{iz} - J_{ix})\sin\epsilon\cos\epsilon + D_{xz}\cos(2\epsilon) \\ \bar{d}_{yz} &= d_{yz} + D_{yz}\cos\epsilon - D_{xy}\sin\epsilon. \end{aligned} \tag{8}$$

Combining (6)–(8), the total torque of the yaw gimbal with respect to z_e-axis is derived as

$$T_{ez} = \bar{J}_{ez}\dot{r}_e + T_{n2} + T_{d2} \tag{9}$$

where T_{n2} and T_{d2} represent the known and unknown cross-coupling dynamics caused by the rotations of base and pitch gimbals, respectively, which are denoted as

$$\begin{aligned} T_{n2} &= (\bar{d}_{yz} - d_{yz})\dot{q}_i - (\bar{d}_{xy} - d_{xy})q_i^2 \\ T_{d2} &= (\bar{J}_{ey} - \bar{J}_{ex})p_eq_e + (\bar{d}_{yz} - d_{yz})p_er_e + \bar{d}_{xy}p_e^2 \\ &\quad + d_{xz}(\dot{p}_e - r_eq_e) + d_{yz}(\dot{q}_e + p_er_e) - d_{xy}q_e^2 \\ &\quad + (\bar{J}_{ez} - J_{ez} - \bar{J}_{ex} + J_{ex} + J_{iy})(p_eq_i - p_eq_e) \\ &\quad + (\bar{d}_{xz} - d_{xz})(\dot{p}_e + r_eq_e - 2r_eq_i). \end{aligned} \tag{10}$$

Since r_i is the system variable we need to control, we can further derive the dynamic model about r_i by using the relationship $r_i = p_e\sin\epsilon + r_e\cos\epsilon$, which yields

$$\bar{J}_{ez}\dot{r}_i = (T_{ez} - T_{n2} - T_{d2})\cos\epsilon + \bar{J}_{ez}(\dot{p}_e\sin\epsilon + p_i\dot{\epsilon}). \tag{11}$$

Combining (4) and (9), the ISP dynamics are attained as

$$\begin{bmatrix} m_{11} & m_{12} \\ m_{21} & m_{22} \end{bmatrix}\begin{bmatrix} \dot{q}_i \\ \dot{r}_i \end{bmatrix} = \begin{bmatrix} f_1(q_i, r_i) \\ f_2(q_i, r_i) \end{bmatrix} + \begin{bmatrix} T_{iy} \\ \bar{T}_{ez} \end{bmatrix} + \begin{bmatrix} d_1(t) \\ d_2(t) \end{bmatrix} \tag{12}$$

where $m_{11} = J_{iy}, m_{21} = D_{yz}\cos^2\epsilon - D_{xy}\sin\epsilon\cos\epsilon, m_{12} = D_{yz}, m_{22} = \bar{J}_{ez}, \bar{T}_{ez} = T_{ez}\cos\epsilon, f_1(q_i, r_i) = -D_{xy}q_ir_i - D_{xz}r_i^2, f_2(q_i, r_i) = (D_{yz}\sin\epsilon\cos\epsilon + D_{xy}\cos^2\epsilon)q_i^2, d_1(t) = -T_{d1}, d_2(t) = -T_{d2}\cos\epsilon + \bar{J}_{ez}(\dot{p}_e\sin\epsilon + p_i\dot{\epsilon})$.

C. Model of PMDC Motor

For the adopted PMDC motors, the electromagnetic torques are expressed as

$$T_{e1} = K_{t1}i_1, \quad T_{e2} = K_{t2}i_2 \tag{13}$$

where K_{tm} is the torque coefficient, i_m is the armature winding current, and the subscripts $m = 1, 2$ denote the models related to the pitch and yaw gimbals (the same below), respectively. Taking account of the external disturbance $T_{fm}(t)$, e.g., the unknown friction torque and load torque, the total torques imposed on the motors of pitch and yaw gimbals are obtained by

$$T_{iy} = T_{e1} - T_{f1}(t), \quad T_{ez} = T_{e2} - T_{f2}(t). \tag{14}$$

Furthermore, the voltage balance equations of the motors of pitch and yaw gimbals are governed by

$$\begin{cases} L_1\dfrac{di_1}{dt} = V_1u_1 - K_{e1}(q_i - q_e) - R_1i_1 \\ L_2\dfrac{di_2}{dt} = V_2u_2 - K_{e2}(r_e - r_b) - R_2i_2 \end{cases} \tag{15}$$

where L_m is the armature winding inductance, V_m is the input dc voltage, u_m is the inverter duty ratio, K_{em} is the back electromotive force (EMF) coefficient, and R_m is the armature winding resistance.

D. Problem Statement

Define the system state vector as $\boldsymbol{x} = [x_1, x_2]^{\mathrm{T}} \in \mathbb{R}^2$ where $x_1 = q_i, x_2 = r_i$. Combining (12)–(15) together, through sets of algebraic operations, the entire dynamic model of the two-axis ISP system can be established as follows:

$$\boldsymbol{M}(\boldsymbol{x})\ddot{\boldsymbol{x}} + \boldsymbol{A}(\boldsymbol{x})\dot{\boldsymbol{x}} + \boldsymbol{B}(\boldsymbol{x}) = \boldsymbol{G}\boldsymbol{u} + \boldsymbol{\Xi}(t) \tag{16}$$

where

$$\boldsymbol{M}(\boldsymbol{x}) = \begin{bmatrix} L_1m_{11} & L_1m_{12} \\ L_2m_{21} & L_2m_{22} \end{bmatrix}, \quad \boldsymbol{A}(\boldsymbol{x}) = \begin{bmatrix} A_{11} & A_{12} \\ A_{21} & A_{22} \end{bmatrix}$$

$$\boldsymbol{B}(\boldsymbol{x}) = \begin{bmatrix} K_{e1}K_{t1}x_1 - R_1f_1(\boldsymbol{x}) \\ K_{e2}K_{t2}x_2 - R_2f_2(\boldsymbol{x}) \end{bmatrix}, \quad \boldsymbol{u} = \begin{bmatrix} u_1 & u_2 \end{bmatrix}^{\mathrm{T}}$$

$$\boldsymbol{G} = \begin{bmatrix} K_{t1}V_1 & 0 \\ 0 & K_{t2}V_2\cos\epsilon \end{bmatrix}, \quad \boldsymbol{\Xi}(t) = \begin{bmatrix} \Xi_1 & \Xi_2 \end{bmatrix}^{\mathrm{T}}$$

with $A_{11} = L_1 D_{xy} x_2 + R_1 m_{11}$, $A_{12} = L_1(2D_{xz}x_2 + D_{xy}x_1) + R_1 m_{12}$, $A_{21} = R_2 m_{21} - L_2[D_{yz}\sin(2\epsilon) + 2D_{xy}\cos^2\epsilon]x_1$, $A_{22} = R_2 m_{22}$, $\Xi_1 = K_{e1}K_{t1}q_e + R_1(d_1 - T_{f1}) + L_1(\dot{d}_1 - \dot{T}_{f1})$, $\Xi_2 = K_{e2}K_{t2}(p_e \sin\epsilon + r_b\cos\epsilon) + R_2(d_2 - T_{f2}\cos\epsilon) + L_2\{\dot{d}_2 - \dot{T}_{f2}\cos\epsilon - \dot{m}_{21}\dot{x}_1 - \dot{m}_{22}\dot{x}_2 + \dot{\epsilon}[D_{yz}\cos(2\epsilon)x_1^2 - D_{xy}\sin(2\epsilon)x_1^2 + (d_2 + f_2(\boldsymbol{x}) - m_{21}\dot{x}_1 - m_{22}\dot{x}_2)\tan\epsilon]\}$.

Here the control inputs are two pulsewidth modulation (PWM) signals ranging from -100% to $+100\%$.

Generally, the parameter uncertainties inevitably exist in practice. As such, it is reasonable to make the assumption that $\boldsymbol{M}(\boldsymbol{x}) = \boldsymbol{M}_o(\boldsymbol{x}) + \Delta\boldsymbol{M}(\boldsymbol{x})$, $\boldsymbol{A}(\boldsymbol{x}) = \boldsymbol{A}_o(\boldsymbol{x}) + \Delta\boldsymbol{A}(\boldsymbol{x})$, $\boldsymbol{B}(\boldsymbol{x}) = \boldsymbol{B}_o(\boldsymbol{x}) + \Delta\boldsymbol{B}(\boldsymbol{x})$, and $\boldsymbol{G} = \boldsymbol{G}_o + \boldsymbol{\Delta G}$, where $\boldsymbol{M}_o(\boldsymbol{x})$, $\boldsymbol{A}_o(\boldsymbol{x})$, $\boldsymbol{B}_o(\boldsymbol{x})$, and $\boldsymbol{G}_o$ are the nominal values of the parameters; $\Delta\boldsymbol{M}(\boldsymbol{x})$, $\Delta\boldsymbol{A}(\boldsymbol{x})$, $\Delta\boldsymbol{B}(\boldsymbol{x})$, and $\Delta\boldsymbol{G}$ represent the perturbations in the system matrices. Then, system dynamics (16) can be rewritten as

$$\boldsymbol{M}_o(\boldsymbol{x})\ddot{\boldsymbol{x}} + \boldsymbol{A}_o(\boldsymbol{x})\dot{\boldsymbol{x}} + \boldsymbol{B}_o(\boldsymbol{x}) = \boldsymbol{G}_o\boldsymbol{u} + \boldsymbol{D}(\boldsymbol{x}, t) \tag{17}$$

where $\boldsymbol{D}(\boldsymbol{x}, t) = \boldsymbol{\Xi}(t) + \Delta\boldsymbol{G}\boldsymbol{u} - \Delta\boldsymbol{M}(\boldsymbol{x})\ddot{\boldsymbol{x}} - \Delta\boldsymbol{A}(\boldsymbol{x})\dot{\boldsymbol{x}} - \Delta\boldsymbol{B}(\boldsymbol{x})$ is composed of unknown cross-couplings, mass imbalance, parameter uncertainties, and external disturbances.

Let $\boldsymbol{x}_d = [x_{1d}, x_{2d}]^{\mathrm{T}} \in \mathbb{R}^2$ be the desired inertial angular rate. Define the tracking error as $\boldsymbol{e} = [e_1, e_2]^{\mathrm{T}} = \boldsymbol{x} - \boldsymbol{x}_d$. In this brief, the control objective is to design a *continuous* terminal sliding mode controller $\boldsymbol{u}$ such that the tracking error $\boldsymbol{e}$ can converge to zero in finite time despite of the multiple disturbances $\boldsymbol{D}(\boldsymbol{x}, t)$ with the assumption that only the inertial angular rates are available.

III. Controller Design

For simplicity of expression, some notations are introduced in the following analysis [17]: $\boldsymbol{x}^\alpha = [x_1^\alpha, x_2^\alpha]^{\mathrm{T}}$, $|\boldsymbol{x}|^\alpha = [|x_1|^\alpha, |x_2|^\alpha]^{\mathrm{T}}$, $\mathrm{sig}^\alpha(\boldsymbol{x}) = [|x_1|^\alpha\mathrm{sign}(x_1), |x_2|^\alpha\mathrm{sign}(x_2)]^{\mathrm{T}}$, $\dot{\boldsymbol{x}}^\alpha = [\dot{x}_1^\alpha, \dot{x}_2^\alpha]^{\mathrm{T}}$, $\mathrm{diag}(\boldsymbol{x}^\alpha) = \mathrm{diag}(x_1^\alpha, x_2^\alpha)$.

A. Robust CTSMC Synthesis

By introducing an auxiliary state vector $\boldsymbol{z} = [\boldsymbol{z}_1^{\mathrm{T}}, \boldsymbol{z}_2^{\mathrm{T}}]^{\mathrm{T}} \in \mathbb{R}^4$ where $\boldsymbol{z}_1 = \boldsymbol{x}$, $\boldsymbol{z}_2 = \dot{\boldsymbol{x}}$, system (17) can be rewritten as

$$\begin{cases} \dot{\boldsymbol{z}}_1 = \boldsymbol{z}_2 \\ \dot{\boldsymbol{z}}_2 = \boldsymbol{M}_o^{-1}(\boldsymbol{z}_1)[-\boldsymbol{B}_o(\boldsymbol{z}_1) + \boldsymbol{G}_o\boldsymbol{u}] + \boldsymbol{H}(\boldsymbol{z}_1, \boldsymbol{z}_2, t) \end{cases} \tag{18}$$

where $\boldsymbol{H}(\boldsymbol{z}_1, \boldsymbol{z}_2, t) = \boldsymbol{M}_o^{-1}(\boldsymbol{z}_1)[-\boldsymbol{A}_o(\boldsymbol{z}_1)\boldsymbol{z}_2 + \boldsymbol{D}(\boldsymbol{z}_1, t)]$ is the redefined lumped uncertainty.

Since only the output $\boldsymbol{z}_1$ is available, we first attempt to estimate $\boldsymbol{z}_2$ and $\boldsymbol{H}$ synchronously. To this end, an HOSMO is constructed for system (18) as

$$\begin{cases} \dot{\hat{\boldsymbol{z}}}_1 &= \hat{\boldsymbol{z}}_2 + \boldsymbol{L}_1\mathrm{sig}^{2/3}(\boldsymbol{e}_{o1}) \\ \dot{\hat{\boldsymbol{z}}}_2 &= \hat{\boldsymbol{H}} + \boldsymbol{M}_o^{-1}(\boldsymbol{z}_1)[-\boldsymbol{B}_o(\boldsymbol{z}_1) + \boldsymbol{G}_o\boldsymbol{u}] + \boldsymbol{L}_2\mathrm{sig}^{1/3}(\boldsymbol{e}_{o1}) \\ \dot{\hat{\boldsymbol{H}}} &= \boldsymbol{L}_3\mathrm{sign}(\boldsymbol{e}_{o1}) \end{cases} \tag{19}$$

where $\boldsymbol{e}_{o1} = \boldsymbol{z}_1 - \hat{\boldsymbol{z}}_1$, $\hat{\boldsymbol{z}}_1$, $\hat{\boldsymbol{z}}_2$, and $\hat{\boldsymbol{H}}$ are the estimates of $\boldsymbol{z}_1$, $\boldsymbol{z}_2$, and $\boldsymbol{H}$, respectively, and $\boldsymbol{L}_i = \mathrm{diag}(l_{i1}, l_{i2})$ for $i = 1, 2, 3$ are the parameters to be designed.

Define the estimation errors as $\boldsymbol{e}_{o2} = \boldsymbol{z}_2 - \hat{\boldsymbol{z}}_2$ and $\boldsymbol{e}_{o3} = \boldsymbol{H} - \hat{\boldsymbol{H}}$. Then, the error dynamics for system (19) are obtained as $\dot{\boldsymbol{e}}_{o1} = \boldsymbol{e}_{o2} - \boldsymbol{L}_1\mathrm{sig}^{2/3}(\boldsymbol{e}_{o1})$, $\dot{\boldsymbol{e}}_{o2} = \boldsymbol{e}_{o3} - \boldsymbol{L}_2\mathrm{sig}^{1/3}(\boldsymbol{e}_{o1})$, $\dot{\boldsymbol{e}}_{o3} = -\boldsymbol{L}_3\mathrm{sign}(\boldsymbol{e}_{o1}) + \dot{\boldsymbol{H}}$.

Remark 2: To guarantee the finite-time convergence of $\boldsymbol{e}_{oi}$, the bound on the derivative of $\boldsymbol{H}$ should be known *a priori*. Since the energy change is always limited in the physical world, it would be reasonable to assume that $\dot{\boldsymbol{H}}$ is bounded by a known constant vector, i.e., $|\{\dot{\boldsymbol{H}}(\boldsymbol{z}_1, \boldsymbol{z}_2, t)\}_i| \le \delta_i, i = 1, 2$.

If the observer gains are assigned as $l_{1i} = \mu_1(\delta_i^{1/3})$, $l_{2i} = \mu_2\mu_1^{1/2}(\delta_i^{2/3})$, $l_{3i} = \mu_3\delta_i$, the error dynamics are governed by

$$\begin{cases} \dot{\boldsymbol{e}}_{o1} = \boldsymbol{e}_{o2} - \mu_1\boldsymbol{\Delta}^{1/3}\mathrm{sig}^{2/3}(\boldsymbol{e}_{o1}) \\ \dot{\boldsymbol{e}}_{o2} = \boldsymbol{e}_{o3} - \mu_2\boldsymbol{\Delta}^{1/2}\mathrm{sig}^{1/2}(\boldsymbol{e}_{o2} - \dot{\boldsymbol{e}}_{o1}) \\ \dot{\boldsymbol{e}}_{o3} = -\mu_3\boldsymbol{\Delta}\mathrm{sign}(\boldsymbol{e}_{o3} - \dot{\boldsymbol{e}}_{o2}) + \dot{\boldsymbol{H}} \end{cases} \tag{20}$$

where $\boldsymbol{\Delta} = \mathrm{diag}(\delta_1, \delta_2)$. It can be inferred from [28] that system (20) is finite-time stable with the proper selection of parameters $\mu_i, i = 1, 2, 3$. That is, there exists finite time t_o such that $\boldsymbol{e}_{oi} \equiv \boldsymbol{0}$ for $\forall t > t_o$ and $\|\boldsymbol{e}_{oi}\|$ is bounded by a positive constant $E_{oi}^{\max}$ for $\forall t \le t_o, i = 1, 2, 3$.

Remark 3: Selections of the parameters μ_i are referred to [28]. For system with relative degree 3, a possible choice is $\mu_1 = 2, \mu_2 = 1.5, \mu_3 = 1.1$. In this sense, δ_i are the only tuning parameters. Generally, the larger values for δ_i are selected, the faster convergence rate of the observer (19) can be obtained; however, undesirable control performances such as the peaking phenomenon and the noise amplification will be caused. To this end, the compromise should be made to balance between the dynamic performance and the measurement noise attenuation in practical applications.

Next, we will design a robust CTSMC algorithm for system (18) based on the estimated information. To begin with, a new terminal sliding surface is designed as

$$\hat{\boldsymbol{s}} = \hat{\boldsymbol{z}}_2 - \dot{\boldsymbol{x}}_d + \int_0^t [\boldsymbol{k}_1\mathrm{sig}^{\alpha_1}(\boldsymbol{e}) + \boldsymbol{k}_2\mathrm{sig}^{\alpha_2}(\hat{\boldsymbol{z}}_2 - \dot{\boldsymbol{x}}_d)]d\tau \tag{21}$$

where $\alpha_1 = (\alpha_2/2 - \alpha_2), \alpha_2 \in (1 - \xi, 1), \xi \in (0, 1)$, and $\boldsymbol{k}_1 = \mathrm{diag}(k_{11}, k_{12})$, $\boldsymbol{k}_2 = \mathrm{diag}(k_{21}, k_{22})$ are selected such that the polynomials $p^2 + k_{2i}p + k_{1i}, i = 1, 2$ are Hurwitz.

Taking the derivative of $\hat{\boldsymbol{s}}$ along system (19), one obtains

$$\begin{aligned} \dot{\hat{\boldsymbol{s}}} = \boldsymbol{M}_o^{-1}(\boldsymbol{z}_1)[-\boldsymbol{B}_o(\boldsymbol{z}_1) + \boldsymbol{G}_o\boldsymbol{u}] + \boldsymbol{L}_2\mathrm{sig}^{1/3}(\boldsymbol{e}_{o1}) \\ + \hat{\boldsymbol{H}} - \ddot{\boldsymbol{x}}_d + \boldsymbol{k}_1\mathrm{sig}^{\alpha_1}(\boldsymbol{e}) + \boldsymbol{k}_2\mathrm{sig}^{\alpha_2}(\hat{\boldsymbol{z}}_2 - \dot{\boldsymbol{x}}_d). \end{aligned} \tag{22}$$

The aim here is to construct a controller $\boldsymbol{u}$ such that the second-order sliding mode occurs in finite time t_r on the sliding surface $\hat{\boldsymbol{s}}$, i.e., $\hat{\boldsymbol{s}} = \dot{\hat{\boldsymbol{s}}} = \boldsymbol{0}, \forall t \ge t_r$. To this end, by setting $\hat{\boldsymbol{s}} = \boldsymbol{0}$, the nominal controller in the absence of uncertainties can be derived as

$$\begin{aligned} \boldsymbol{u}_{n1} = \boldsymbol{G}_o^{-1}\{\boldsymbol{B}_o(\boldsymbol{z}_1) + \boldsymbol{M}_o(\boldsymbol{z}_1)[\ddot{\boldsymbol{x}}_d - \boldsymbol{L}_2\mathrm{sig}^{1/3}(\boldsymbol{e}_{o1})] \\ - \boldsymbol{M}_o(\boldsymbol{z}_1)[\boldsymbol{k}_1\mathrm{sig}^{\alpha_1}(\boldsymbol{e}) + \boldsymbol{k}_2\mathrm{sig}^{\alpha_2}(\hat{\boldsymbol{z}}_2 - \dot{\boldsymbol{x}}_d)]\}. \end{aligned} \tag{23}$$

To endow the robustness against uncertainties, the disturbance compensation term is incorporated as

$$\boldsymbol{u}_{d1} = -\boldsymbol{G}_o^{-1}\boldsymbol{M}_o(\boldsymbol{z}_1)\hat{\boldsymbol{H}}. \tag{24}$$

Moreover, a reaching element using the fast terminal sliding manifold is employed to guarantee the fast convergence rate [17], which is designed as

$$\boldsymbol{u}_{s1} = -\boldsymbol{G}_o^{-1}\boldsymbol{M}_o(\boldsymbol{z}_1)[\boldsymbol{\lambda}_1\hat{\boldsymbol{s}} + \boldsymbol{\lambda}_2\mathrm{sig}^{\beta}(\hat{\boldsymbol{s}})] \tag{25}$$

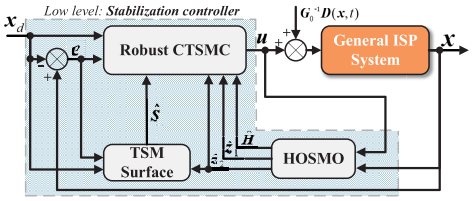

Fig. 3. Implementation diagram of the proposed method.

where $\boldsymbol{\lambda}_i = \text{diag}(\lambda_{i1}, \lambda_{i2}), i = 1, 2$ are positive constants and $\beta \in (0, 1)$.

With the combination of (23)–(25), the proposed control law is designed as

$$\boldsymbol{u} = \boldsymbol{u}_{n1} + \boldsymbol{u}_{s1} + \boldsymbol{u}_{d1}. \tag{26}$$

The implementation diagram of the proposed control method is depicted in Fig. 3.

Remark 4: It can be observed from (23) that the effects of cross-couplings and mass imbalance, i.e., $\boldsymbol{B}_o(\boldsymbol{z}_1)$ are explicitly considered in the controller design, which reduces the online observation burden of the sliding mode observer (19). Moreover, by utilizing the joint estimations of the system state $\boldsymbol{z}_2$ and the uncertain dynamics $\boldsymbol{H}$, an output-feedback based CTSMC approach is essentially realized to enhance the disturbance rejection ability of the ISPs.

B. Stability Analysis

Lemma 1 plays a crucial role in the development of the main result of this brief.

Lemma 1 [29]: Consider the following system:

$$\dot{x}_i = x_{i+1}, \quad i = 1, \ldots, n-1, \ \dot{x}_n = u. \tag{27}$$

There exists a constant $\xi \in (0, 1)$, for any $\alpha \in (1 - \xi, 1)$, system (27) is finite-time stable under the control law

$$u = -k_1 \text{sig}^{\alpha_1}(x_1) - \cdots - k_n \text{sig}^{\alpha_n}(x_n) \tag{28}$$

where $\alpha_{i-1} = (\alpha_i \alpha_{i+1}/2\alpha_{i+1} - \alpha_i), i = 2, \ldots, n, \alpha_{n+1} = 1, \alpha_n = \alpha$, and $k_1, \ldots, k_n$ are selected such that the polynomial $s^n + k_n s^{n-1} + \ldots + k_2 s + k_1$ is Hurwitz.

The Lyapunov theory is employed to prove the stability and convergence of the closed-loop system.

Theorem 1: For the two-axis ISP system (17), under the proposed CTSMC method consisting of the observer (19), the sliding surface (21), and the control law (26), the tracking error $\boldsymbol{e}$ of the inertial angular rates will converge to zero in finite time.

Proof: The detailed proof can be found in the Appendix.

IV. Experimental Implementation and Performance Validation

To validate the effectiveness of the proposed method, the experimental tests are conducted in this section. The experimental setup of the two-axis ISP system is shown in Fig. 4, comprising the pitch-yaw gimbals, the digital signal processor (DSP) control unit, the signal measurement unit, and the motion imitation unit. The angular rates are measured by a two-axis FOG (VG091A) and converted through the analog-to-digital chip (AD7656) with 16-bit resolution. The optical encoder (BEC60-S10-17-5V) with 17-bit resolution is employed to measure the relative angle. In order to imitate the practical working environment, an one-axis motion carrier is employed to generate the yaw channel rotation. The parameters of the adopted PMDC motors are: $V_m = 27$ V, $R_m = 9.8\ \Omega$, $L_m = 6.5$ mH, $K_{tm} = 0.43$ N·m/A, $K_{em} = 0.21$ V/(rad/s). The nominal values of the inertial matrices of pitch and yaw gimbals are: $\boldsymbol{J}_{IN} = \text{diag}\ (0.135,\ 0.192,\ 0.135)\ \text{kg} \cdot \text{m}^2$ and $\boldsymbol{J}_{EN} = \text{diag}\ (0.174,\ 0.174,\ 0.158)\ \text{kg} \cdot \text{m}^2$, respectively. The sampling period of the control system is set as $100\mu s$.

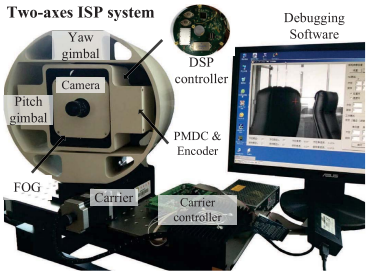

Fig. 4. Experimental setup.

Two control algorithms are implemented for the performance comparisons:

1) The TSMC approach in [18] with the boundary layer (BL) method (CTSMC-BL), where the BL approach is employed to reduce the chattering, is designed as

$$\begin{cases} \boldsymbol{u} = \boldsymbol{u}_{n2} + \boldsymbol{u}_{s2}, \\ \boldsymbol{u}_{n2} = \boldsymbol{G}_o^{-1}[\boldsymbol{A}_o(\boldsymbol{x})\dot{\boldsymbol{x}} + \boldsymbol{B}_o(\boldsymbol{x}) + \boldsymbol{M}_o(\boldsymbol{x})\ddot{\boldsymbol{x}}_d \\ \qquad\qquad -\boldsymbol{M}_o(\boldsymbol{x})\boldsymbol{c}^{-1}\alpha^{-1}\text{sig}^{2-\alpha}(\dot{\boldsymbol{e}})] \\ \boldsymbol{u}_{s2} = -\phi \boldsymbol{G}_o^{-1}\boldsymbol{M}_o(\boldsymbol{x})\text{sat}(\boldsymbol{s}, \sigma) \\ \boldsymbol{s} = \boldsymbol{e} + \boldsymbol{c}\text{sig}^{\alpha}(\dot{\boldsymbol{e}}) \end{cases} \tag{29}$$

where $\text{sat}(\boldsymbol{s}, \sigma) = [\text{sat}_1(s_1, \sigma), \text{sat}_2(s_2, \sigma)]^{\text{T}}$ is the saturation function, and $\text{sat}_i(s_i, \sigma) = s_i/|s_i|$, if $|s_i| > \sigma$, and $\text{sat}_i(s_i, \sigma) = s_i/\sigma$, else if $|s_i| \le \sigma$, σ is a positive constant close to zero; ϕ is the switching gain, designed as $\phi > \sup_{t>0} \|\boldsymbol{M}_o^{-1}(\boldsymbol{x})\boldsymbol{D}(\boldsymbol{x}, t)\|$, $\boldsymbol{c} = \text{diag}(c_1, c_2), c_1, c_2 > 0$, and $\alpha \in (1, 2)$.

Remark 5: For the choice of the BL width parameter σ, the smaller the selected value, the better the robustness, but the more serious the control chattering [30]. On the other hand, choosing an overlarge ϕ will cause the peaking phenomenon even the BL method is employed. To this end, the parameters ϕ and σ should be properly chosen to balance the dynamic response and robust performance.

2) The ADRC approach in [12] is designed as

$$\begin{cases} \dot{\hat{\boldsymbol{z}}}_1 = \hat{\boldsymbol{z}}_2 + \boldsymbol{\beta}_1(\boldsymbol{z}_1 - \hat{\boldsymbol{z}}_1) \\ \dot{\hat{\boldsymbol{z}}}_2 = \hat{\boldsymbol{H}} + \boldsymbol{M}_o^{-1}(\boldsymbol{z}_1)[-\boldsymbol{B}_o(\boldsymbol{z}_1) + \boldsymbol{G}_o\boldsymbol{u}] + \boldsymbol{\beta}_2(\boldsymbol{z}_1 - \hat{\boldsymbol{z}}_1) \\ \dot{\hat{\boldsymbol{H}}} = \boldsymbol{\beta}_3(\boldsymbol{z}_1 - \hat{\boldsymbol{z}}_1) \\ \boldsymbol{u} = \boldsymbol{G}_o^{-1}\boldsymbol{M}_o(\boldsymbol{z}_1)[\boldsymbol{M}_o^{-1}(\boldsymbol{z}_1)\boldsymbol{B}_o(\boldsymbol{z}_1) + \ddot{\boldsymbol{x}}_d \\ \qquad\qquad -\hat{\boldsymbol{H}} - \boldsymbol{k}_p(\boldsymbol{z}_1 - \boldsymbol{x}_d) - \boldsymbol{k}_d(\hat{\boldsymbol{z}}_2 - \dot{\boldsymbol{x}}_d)]. \end{cases} \tag{30}$$

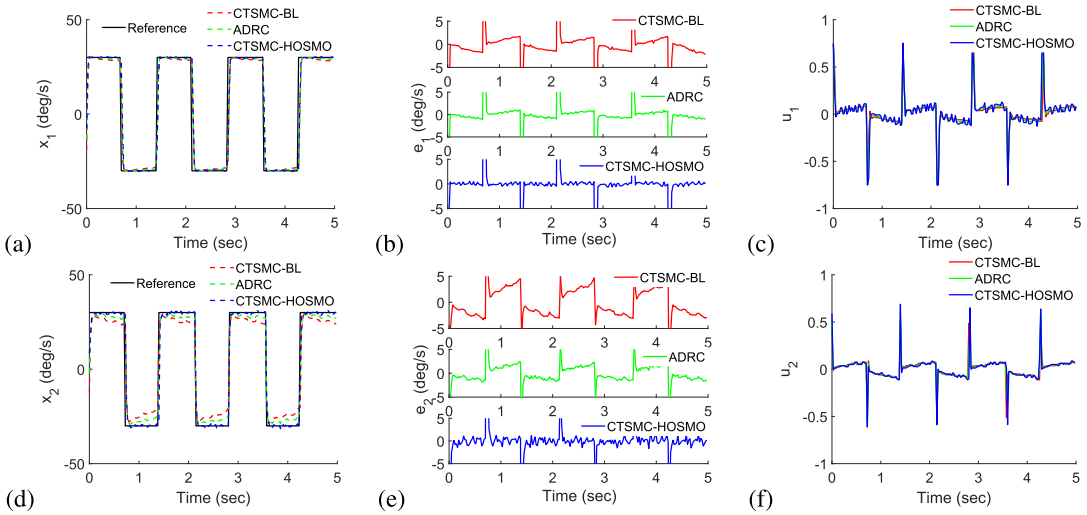

Fig. 5. Experimental response curves in Case I. (a) Angular rate x_1. (b) Tracking error e_1. (c) Control duty ratio u_1. (d) Angular rate x_2. (e) Tracking error e_2. (f) Control duty ratio u_2.

where $\boldsymbol{\beta}_i, i = 1, 2, 3$ are the observer gains and $\boldsymbol{k}_p, \boldsymbol{k}_d$ are the feedback control gains to be designed.

All the algorithms are implemented on a DSP chip model TMS320F28335 with C-program development. The comparative experiments are conducted in two different cases: tracking the step signals and the sinusoidal signals, respectively. During the testing process, the carrier is forced to do reciprocating motion on the yaw channel and the motion trajectory is set as trapezoid curve. On this occasion, for the pitch gimbal, the coupling induced by the relative rotation between pitch and yaw gimbals has a major impact on control performances, while for the yaw gimbal, the performance is also influenced by the carrier motion in addition to the above factor.

It is well known that there are usually many conflicts/constraints in control system design and tuning (e.g., tracking versus disturbance rejection and nominal performance versus robustness). To fulfill a fair comparison, one reasonable manner is to tune the controllers that obtain some similar performance specifications and then compare with the others. Given this fact, we first tune the control parameters of each controller such that the inertial angular rate profiles have the similar transient performances like settling times and overshoots. Naturally, the robustness and disturbance rejection performances are then relatively fair compared. For the CTSMC-BL method (29), the parameters are set as: $\alpha = 1.8$, $\boldsymbol{c} = \text{diag}(0.02, 0.03), \phi = 115, \sigma = 0.01$. For the ADRC method (30), the parameters are set as: $\boldsymbol{k}_p = \text{diag}(750, 820)$, $\boldsymbol{k}_d = \text{diag}(37, 49)$, $\boldsymbol{\beta}_1 = \text{diag}(30, 50)$, $\boldsymbol{\beta}_2 = \text{diag}(300, 460)$, $\boldsymbol{\beta}_3 = \text{diag}(950, 1450)$. For the proposed control approach (26), the parameters are set as: $\boldsymbol{k}_1 = \text{diag}(784, 961)$, $\boldsymbol{k}_2 = \text{diag}(46, 52)$, $\alpha_1 = 0.18$, $\alpha_2 = 0.3$, $\boldsymbol{\lambda}_1 = \text{diag}(390, 420)$, $\boldsymbol{\lambda}_2 = \text{diag}(235, 275)$, $\boldsymbol{\Delta} = \text{diag}(600, 1000)$.

A. Case I-Step Signal Tracking

Under this case, the desired angular rates of the LOS on pitch and yaw channels are both set as the square-wave signals with the amplitude of 30°/s. The experimental response curves are shown in Fig. 5.

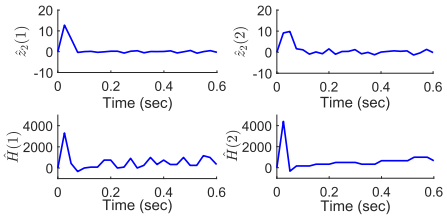

Fig. 6. Observation results in Case I.

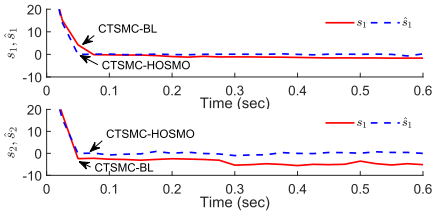

Fig. 7. Sliding mode variables in Case I.

It can be observed that the proposed robust CTSMC approach possesses better disturbance rejection performance in comparison to the CTSMC-BL and ADRC approaches. As shown in Fig. 5(e), for the yaw gimbal, the offset caused by the carrier motion and couplings is almost removed by using the proposed control scheme, whereas it can only guarantee the output tracking errors converge to a bounded region by means of the other two methods.

The observation results of the HOSMO during one period are shown in Fig. 6, including the angular acceleration $\hat{\boldsymbol{z}}_2$ and the lumped uncertainty $\hat{\boldsymbol{H}}$. Fig. 7 shows that in the presence of cross-couplings and mass imbalance, the system states can reach the sliding surfaces $\hat{s}_1 = \hat{s}_2 = 0$ quickly, whereas it can hardly reach the sliding surface $s_1 = s_2 = 0$ by means of the BL-based method.

B. Case II-Sinusoidal Signal Tracking

Here the desired angular rates of the pitch and yaw channels are both set as the time-varying sinusoidal signals with the

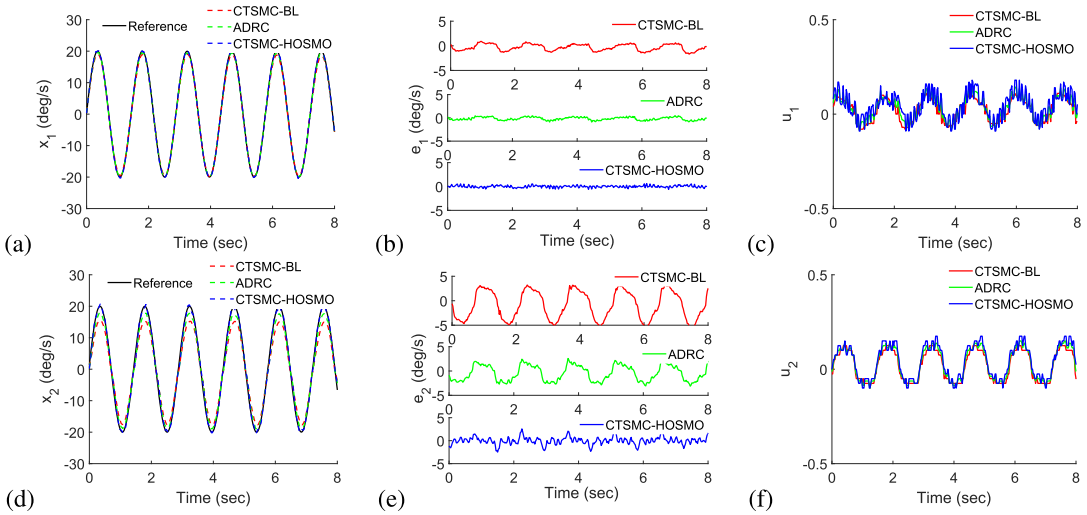

Fig. 8. Experimental response curves in Case II. (a) Angular rate x_1. (b) Tracking error e_1. (c) Control duty ratio u_1. (d) Angular rate x_2. (e) Tracking error e_2. (f) Control duty ratio u_2.

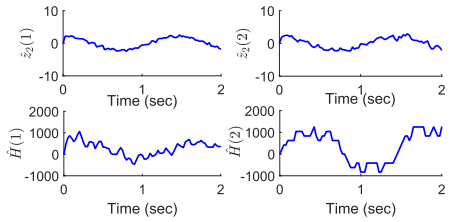

Fig. 9. Observation results in Case II.

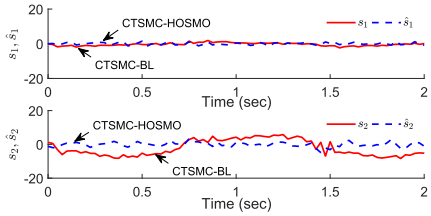

Fig. 10. Sliding mode variables in Case II.

TABLE I
PERFORMANCE INDEXES UNDER THREE CONTROL SCHEMES

		Pitch Gimbal (deg/s)		Yaw Gimbal (deg/s)	
	Control scheme	MA	RMS	MA	RMS
Case I	CTSMC-BL	1.82	0.586	3.34	0.962
	ADRC	1.03	0.392	2.57	0.735
	CTSMC-HOSMO	0.52	0.254	1.41	0.684
Case II	CTSMC-BL	1.72	0.647	5.42	2.866
	ADRC	1.16	0.428	3.94	1.455
	CTSMC-HOSMO	0.64	0.231	2.57	0.943

amplitude of 20°/s and the rotational frequency of 0.7Hz. The experimental response curves are shown in Fig. 8.

As shown in Fig. 8(b) and (e), with the assistance of the designed HOSMO, even for tracking the sinusoidal signals, the uncertainties and disturbances are almost compensated by the proposed control scheme. Owing to the finite-time convergence property of the proposed controller, the transient responses of the angular rates also perform very well. While for the ADRC approach, the tracking performance is evidently affected by the multiple time-varying disturbances. The observation results, in this case, are shown in Figs. 9, and 10 shows the dynamic curves of the sliding mode variables.

In order to gain more insight quantitatively, the performance indexes including the maximum absolute (MA) value and the root-mean-squared (rms) value of the output tracking errors are presented in Table I. It can be explicitly observed from the comparative results that the proposed scheme provides the best control performance among the three control strategies.

V. CONCLUSION

In this brief, a robust CTSMC approach has been proposed to achieve a higher control precision for the two-axis ISP. Different from most of the existing results, we have analyzed the modeling and control issues under the case when the mass distribution of an ISP is nonsymmetrical with respect to the mass center. To avoid the weakness of the traditional TSMC, the uncertainties caused by cross-couplings, mass imbalance, and other unmodeled dynamics as well as the unmeasured angular accelerations were reconstructed by a HOSMO. The effectiveness of the proposed control approach in terms of control accuracy and robustness has been verified by the experimental results.

APPENDIX
PROOF OF THEOREM 1

Proof: The proof is divided into three steps. First, the sliding mode variable $\hat{\boldsymbol{s}}$ is finite-time stable. Second, the system variables $\hat{\boldsymbol{s}}, \boldsymbol{e}$, and $\hat{\boldsymbol{z}}_2$ will not escape to infinity in any given time interval $[0, t_e]$ with $t_e > t_o$. Third, the tracking error $\boldsymbol{e}$ will converge to zero in finite time.

Step 1 (Finite-Time Stability of Sliding Mode Variable): By substituting the control law (26) into (22), one obtains $\dot{\hat{\boldsymbol{s}}} = -\boldsymbol{\lambda}_1\hat{\boldsymbol{s}} - \boldsymbol{\lambda}_2 \mathrm{sig}^{\beta}(\hat{\boldsymbol{s}})$. Consider the Lyapunov function as

$V_s(\hat{\boldsymbol{s}}) = \hat{\boldsymbol{s}}^{\mathrm{T}}\hat{\boldsymbol{s}}/2$. Taking the derivative of V_s yields

$$\dot{V}_s = -\hat{\boldsymbol{s}}^{\mathrm{T}}\boldsymbol{\lambda}_1\hat{\boldsymbol{s}} - \hat{\boldsymbol{s}}^{\mathrm{T}}\boldsymbol{\lambda}_2\mathrm{sig}^{\beta}(\hat{\boldsymbol{s}}) \le -2\underline{\lambda}_1 V_s - \sqrt{2}^{\beta+1}\underline{\lambda}_2 V_s^{\frac{\beta+1}{2}} \quad (31)$$

where $\underline{\lambda}_1 = \min\{\lambda_{1i}\}$, $\underline{\lambda}_2 = \min\{\lambda_{2i}\}, i = 1, 2$. Inequality (31) reveals that $\hat{\boldsymbol{s}}$ will converge to zero in finite time [17], i.e., there exists a time constant t_r such that the second-order sliding mode $\hat{\boldsymbol{s}} = \dot{\hat{\boldsymbol{s}}} = \boldsymbol{0}$ occurs for $\forall t \ge t_r$.

Step 2 (Finite-Time Boundness of System States): Define a finite time bounded function as

$$V_b(\hat{\boldsymbol{s}}, \boldsymbol{e}, \hat{\boldsymbol{z}}_2, t) = \frac{1}{2}[\hat{\boldsymbol{s}}^{\mathrm{T}}\hat{\boldsymbol{s}} + \boldsymbol{e}^{\mathrm{T}}\boldsymbol{e} + (\hat{\boldsymbol{z}}_2 - \dot{\boldsymbol{x}}_d)^{\mathrm{T}}(\hat{\boldsymbol{z}}_2 - \dot{\boldsymbol{x}}_d)]. \quad (32)$$

By substituting the control law (26) into (19), we have

$$\dot{\hat{\boldsymbol{z}}}_2 = \ddot{\boldsymbol{x}}_d - \boldsymbol{k}_1\mathrm{sig}^{\alpha_1}(\boldsymbol{e}) - \boldsymbol{k}_2\mathrm{sig}^{\alpha_2}(\hat{\boldsymbol{z}}_2 - \dot{\boldsymbol{x}}_d) - \boldsymbol{\lambda}_1\hat{\boldsymbol{s}} - \boldsymbol{\lambda}_2\mathrm{sig}^{\beta}(\hat{\boldsymbol{s}}). \quad (33)$$

Taking the derivative of V_b yields

$$\begin{aligned}\dot{V}_b &= \hat{\boldsymbol{s}}^{\mathrm{T}}\dot{\hat{\boldsymbol{s}}} + \boldsymbol{e}^{\mathrm{T}}\dot{\boldsymbol{e}} + (\hat{\boldsymbol{z}}_2 - \dot{\boldsymbol{x}}_d)^{\mathrm{T}}(\dot{\hat{\boldsymbol{z}}}_2 - \ddot{\boldsymbol{x}}_d)\\ &= -\hat{\boldsymbol{s}}^{\mathrm{T}}\boldsymbol{\lambda}_1\hat{\boldsymbol{s}} - \hat{\boldsymbol{s}}^{\mathrm{T}}\boldsymbol{\lambda}_2\mathrm{sig}^{\beta}(\hat{\boldsymbol{s}}) + \boldsymbol{e}^{\mathrm{T}}(\hat{\boldsymbol{z}}_2 - \dot{\boldsymbol{x}}_d + \boldsymbol{e}_{o2})\\ &\quad - (\hat{\boldsymbol{z}}_2 - \dot{\boldsymbol{x}}_d)^{\mathrm{T}}[\boldsymbol{k}_1\mathrm{sig}^{\alpha_1}(\boldsymbol{e}) + \boldsymbol{k}_2\mathrm{sig}^{\alpha_2}(\hat{\boldsymbol{z}}_2 - \dot{\boldsymbol{x}}_d)]\\ &\quad - (\hat{\boldsymbol{z}}_2 - \dot{\boldsymbol{x}}_d)^{\mathrm{T}}[\boldsymbol{\lambda}_1\hat{\boldsymbol{s}} + \boldsymbol{\lambda}_2\mathrm{sig}^{\beta}(\hat{\boldsymbol{s}})]. \end{aligned} \quad (34)$$

For the vectors $\boldsymbol{x}, \boldsymbol{y} \in \mathbb{R}^n$, we have $|\boldsymbol{x}^{\mathrm{T}}\boldsymbol{y}| \le (1/2)(\|\boldsymbol{x}\|^2 + \|\boldsymbol{y}\|^2)$, $|\boldsymbol{x}^{\mathrm{T}}\mathrm{sig}^{\beta}(\boldsymbol{y})| \le (n/2) + \|\boldsymbol{x}\|^2 + (1/2)\|\boldsymbol{y}\|^2$ where $\beta \in (0, 1)$. With the properties, (34) can be further estimated by

$$\begin{aligned}\dot{V}_b &\le \frac{\bar{\lambda}_1 + \bar{\lambda}_2}{2}\|\hat{\boldsymbol{s}}\|^2 + \frac{1 + 2\bar{k}_1 + \bar{\lambda}_1 + 2\bar{\lambda}_2}{2}\|\hat{\boldsymbol{z}}_2 - \dot{\boldsymbol{x}}_d\|^2\\ &\quad + \frac{2 + \bar{k}_1}{2}\|\boldsymbol{e}\|^2 + \frac{\|\boldsymbol{e}_{o2}\|^2}{2} + \bar{k}_1 + \bar{\lambda}_2 \le K_V V_b + L_V \end{aligned} \quad (35)$$

where $\bar{k}_1 = \max\{k_{1i}\}$, $\bar{\lambda}_1 = \max\{\lambda_{1i}\}$, $\bar{\lambda}_2 = \max\{\lambda_{2i}\}$, $i = 1, 2$, $K_V = \max\{1 + 2\bar{k}_1 + \bar{\lambda}_1 + 2\bar{\lambda}_2, 2 + \bar{k}_1\}$ and $L_V = (1/2)(E_{o2}^{\max})^2 + \bar{k}_1 + \bar{\lambda}_2$. It follows from (35) that the solution of V_b satisfies $V_b \le (L_V/K_V) + (V_b(0) - (L_V/K_V))e^{K_V t}, t \le t_o$. This indicates that the system variables $\hat{\boldsymbol{s}}, \boldsymbol{e}$, and $\hat{\boldsymbol{z}}_2$ are bounded in the given time interval $t \in [0, t_e]$, $t_e > t_o$.

Step 3: (Finite-Time Convergence of Output Tracking Error): Define a bounded time constant $T = \max\{t_o, t_r\}$. When $t > T, \hat{\boldsymbol{s}} = \dot{\hat{\boldsymbol{s}}} = \boldsymbol{0}$ and $\hat{\boldsymbol{z}}_2 = \boldsymbol{z}_2$ are achieved. With this in mind, system (33) reduces to $\dot{\hat{\boldsymbol{z}}}_2 - \ddot{\boldsymbol{x}}_d = -\boldsymbol{k}_1\mathrm{sig}^{\alpha_1}(\boldsymbol{e}) - \boldsymbol{k}_2\mathrm{sig}^{\alpha_2}(\hat{\boldsymbol{z}}_2 - \dot{\boldsymbol{x}}_d) \Rightarrow \ddot{\boldsymbol{e}} = -\boldsymbol{k}_1\mathrm{sig}^{\alpha_1}(\boldsymbol{e}) - \boldsymbol{k}_2\mathrm{sig}^{\alpha_2}(\dot{\boldsymbol{e}})$.

By Lemma 1, we can conclude that the tracking error $\boldsymbol{e}$ will converge to zero in finite time. This completes the proof. ∎

REFERENCES

[1] M. K. Masten, "Inertially stabilized platforms for optical imaging systems," *IEEE Control Syst.*, vol. 28, no. 1, pp. 47–64, Feb. 2008.

[2] J. M. Hilkert, "Inertially stabilized platform technology concepts and principles," *IEEE Control Syst. Mag.*, vol. 28, no. 1, pp. 26–46, Feb. 2008.

[3] Z. Hurák and M. Řezáč, "Image-based pointing and tracking for inertially stabilized airborne camera platform," *IEEE Trans. Control Syst. Technol.*, vol. 20, no. 5, pp. 1146–1159, Sep. 2012.

[4] B. Ekstrand, "Equations of motion for a two-axes gimbal system," *IEEE Trans. Aerosp. Electron. Syst.*, vol. 37, no. 3, pp. 1083–1091, Jul. 2001.

[5] Y. Zhang *et al.*, "Fuzzy-PID control for the position loop of aerial inertially stabilized platform," *Aerosp. Sci. Technol.*, vol. 36, pp. 21–26, Jul. 2014.

[6] X. Zhou, Y. Jia, Q. Zhao, and T. Cai, "Dual-rate-loop control based on disturbance observer of angular acceleration for a three-axis aerial inertially stabilized platform," *ISA Trans.*, vol. 63, pp. 288–298, July. 2016.

[7] J. Fang, R. Yin, and X. Lei, "An adaptive decoupling control for three-axis gyro stabilized platform based on neural networks," *Mechatronics*, vol. 27, pp. 38–46, Apr. 2015.

[8] X. Lei, Y. Zou, and F. Dong, "A composite control method based on the adaptive RBFNN feedback control and the ESO for two-axis inertially stabilized platforms," *ISA Trans.*, vol. 59, pp. 424–433, Nov. 2015.

[9] X. Zhou, H. Zhang, and R. Yu, "Decoupling control for two-axis inertially stabilized platform based on an inverse system and internal model control," *Mechatronics*, vol. 24, no. 8, pp. 1203–1213, Dec. 2014.

[10] A. Safa and R. Y. Abdolmalaki, "Robust output feedback tracking control for inertially stabilized platforms with matched and unmatched uncertainties," *IEEE Trans. Control Syst. Technol.*, vol. 27, no. 1, pp. 118–131, Jan. 2019. doi: 10.1109/TCST.2017.2761324.

[11] F. Dong, X. Lei, and W. Chou, "A dynamic model and control method for a two-axis inertially stabilized platform," *IEEE Trans. Ind. Electron.*, vol. 64, no. 1, pp. 432–439, Jan. 2017.

[12] B. Ahi and A. Nobakhti, "Hardware implementation of an ADRC controller on a gimbal mechanism," *IEEE Trans. Control Syst. Technol.*, vol. 26, no. 6, pp. 2268–2275, Nov. 2018. doi: 10.1109/TCST.2017.2746059.

[13] H. Li, S. Zheng, and X. Ning, "Precise control for gimbal system of double gimbal control moment gyro based on cascade extended state observer," *IEEE Trans. Ind. Electron.*, vol. 64, no. 6, pp. 4653–4661, Jun. 2017.

[14] B. Xiao, Q. Hu, and Y. Zhang, "Finite-time attitude tracking of spacecraft with fault-tolerant capability," *IEEE Trans. Control Syst. Technol.*, vol. 23, no. 4, pp. 1338–1350, Jul. 2015.

[15] S. Li, H. Sun, J. Yang, and X. Yu, "Continuous finite-time output regulation for disturbed systems under mismatching condition," *IEEE Trans. Autom. Control*, vol. 60, no. 1, pp. 277–282, Jan. 2015.

[16] Q. Hu and B. Jiang, "Continuous finite-time attitude control for rigid spacecraft based on angular velocity observer," *IEEE Trans. Aerosp. Electron. Syst.*, vol. 54, no. 3, pp. 1082–1092, Jun. 2018. doi: 10.1109/TAES.2017.2773340.

[17] S. Yu, X. Yu, B. Shirinzadeh, and Z. Man, "Continuous finite-time control for robotic manipulators with terminal sliding mode," *Automatica*, vol. 41, no. 11, pp. 1957–1964, Nov. 2005.

[18] Y. Feng, X. Yu, and Z. Man, "Non-singular terminal sliding mode control of rigid manipulators," *Automatica*, vol. 38, no. 12, pp. 2159–2167, 2002.

[19] S.-Y. Chen and F.-J. Lin, "Robust nonsingular terminal sliding-mode control for nonlinear magnetic bearing system," *IEEE Trans. Control Syst. Technol.*, vol. 19, no. 3, pp. 636–643, May 2011.

[20] Y. Wang, L. Gu, Y. Xu, and X. Cao, "Practical tracking control of robot manipulators with continuous fractional-order nonsingular terminal sliding mode," *IEEE Trans. Ind. Electron.*, vol. 63, no. 10, pp. 6194–6204, Oct. 2016.

[21] J. Yang, S. Li, J. Su, and X. Yu, "Continuous nonsingular terminal sliding mode control for systems with mismatched disturbances," *Automatica*, vol. 49, no. 7, pp. 2287–2291, 2013.

[22] M. Jin, J. Lee, and K. K. Ahn, "Continuous nonsingular terminal sliding-mode control of shape memory alloy actuators using time delay estimation," *IEEE/ASME Trans. Mechatronics*, vol. 20, no. 2, pp. 899–909, Apr. 2015.

[23] Y. Wang, F. Yan, S. Jiang, and B. Chen, "Time delay control of cable-driven manipulators with adaptive fractional-order nonsingular terminal sliding mode," *Adv. Eng. Softw.*, vol. 121, pp. 13–25, Jul. 2018.

[24] W.-H. Chen, "Disturbance observer based control for nonlinear systems," *IEEE/ASME Trans. Mechatronics*, vol. 9, no. 4, pp. 706–710, Dec. 2004.

[25] W.-H. Chen, J. Yang, L. Guo, and S. Li, "Disturbance-observer-based control and related methods—An overview," *IEEE Trans. Ind. Electron.*, vol. 63, no. 2, pp. 1083–1095, Feb. 2016.

[26] S. Li, J. Yang, W.-H. Chen, and X. Chen, *Disturbance Observer-Based Control: Methods and Applications*. Baton Rouge, LA, USA: CRC Press, 2014.

[27] J. Yang, W.-H. Chen, S. Li, L. Guo, and Y. Yan, "Disturbance/uncertainty estimation and attenuation techniques in PMSM drives—A survey," *IEEE Trans. Ind. Electron.*, vol. 64, no. 4, pp. 3273–3285, Apr. 2017.

[28] A. Levant, "Higher-order sliding modes, differentiation and output-feedback control," *Int. J. Control*, vol. 76, nos. 9–10, pp. 924–941, 2003.

[29] S. P. Bhat and D. S. Bernstein, "Geometric homogeneity with applications to finite-time stability," *Math. Control, Signals Syst.*, vol. 17, no. 2, pp. 101–127, Jun. 2005.

[30] V. I. Utkin, *Sliding Modes in Control and Optimization*. Berlin, Germany: Springer, 1992.